

Gunnar Brix, PhD
Malte L. Bahner, MD
Ulf Hoffmann, PhD
Andrea Horvath, MS
Wolfgang Schreiber, PhD

Index terms:

Blood, flow dynamics, 20.12114, 57.12113
Computed tomography (CT), contrast enhancement, 20.12114, 57.12113
Computed tomography (CT), diffusion study, 20.12114
Head and neck neoplasms, 20.37, 997.33

Radiology 1999; 210:269–276

¹ From the German Cancer Research Center, Heidelberg. Received January 28, 1998; revision requested March 6; revision received May 21; accepted July 20. **Address reprint requests to** G.B., Institut für Strahlenhygiene, BFS, Ingolstädter Landstrasse 1, 85764 Oberschleissheim, Germany.

© RSNA, 1999

Author contributions:

Guarantor of integrity of entire study, G.B.; study concepts, G.B., W.S.; study design, G.B., M.L.B.; definition of intellectual content, G.B., M.L.B.; literature research, G.B.; clinical studies, M.L.B.; data acquisition, M.L.B.; data analysis, G.B., U.H., A.H.; manuscript preparation and editing, G.B.; manuscript review, M.L.B., U.H., A.H., W.S.

Regional Blood Flow, Capillary Permeability, and Compartmental Volumes: Measurement with Dynamic CT—Initial Experience¹

Sequential computed tomographic scanning was performed in patients with neck tumors after contrast material administration. For data analysis, a pharmacokinetic two-compartment model was employed that takes into account both capillary blood supply and bidirectional diffusion of the contrast agent across the capillary wall. This approach offers the possibility to quantitatively characterize tissue microcirculation with regional blood flow, capillary permeability, and relative compartmental volumes.

For a long time, physiologic tissue parameters could be obtained only with nuclear medicine imaging techniques. Recent advances in computed tomography (CT) and magnetic resonance (MR) imaging technology, however, have helped to reduce scanning times and image repetition rates and, thus, have sped up the introduction of dynamic CT and MR imaging techniques into clinical routine. Since the temporal change of the tissue signal after the administration of a contrast medium is related to the local capillary blood supply and the extravasation of the contrast medium into the surrounding tissue, dynamic imaging procedures can be used to assess tissue microcirculation. Up to now, two major strategies for the analysis of sequential CT scans after administration of a rapid contrast agent bolus have been used.

The theoretic concepts of the first technique, which is based on principles of indicator dilution theory and deconvolution analysis, were described by Axel in 1980 (1) and worked out by Berninger et

al (2) and Norman et al (3) in 1981. This approach made it possible to determine the mean transit time of a contrast agent bolus and the regional cerebral blood flow in structurally intact brain tissue (ie, in tissue regions without a disrupted blood-brain barrier) (4,5). Most recently, it was also successfully applied to the analysis of dynamic MR images of the brain (6–9). The application of the indicator dilution theory, however, is limited because contrast media frequently applied in CT and MR imaging studies do not remain within the intravascular space of brain tissues, with disruption of the blood-brain barrier, or in extracranial tissues.

An alternative approach for the analysis of contrast enhancement in extracranial tissues was presented in a pioneering study by Miles in 1991 (10). By adapting a nuclear medicine data processing technique (11), Miles showed that tissue perfusion can be determined from the maximum gradient of the attenuation-time course, measured in the examined tissue region, divided by the peak signal enhancement in the aorta. This relationship is derived under the assumption that no venous outflow and/or extravasation of the contrast medium has occurred before the steepest gradient is determined (12). Although this approach was successfully used to quantify tissue perfusion in the kidney, liver, pancreas, and spleen (10,12–14), it should be extended to take into account also bidirectional diffusion of the contrast medium across the capillary wall to allow a more comprehensive characterization of tissue microcirculation.

This is of special interest for the detection and biologic characterization of tumors, since tumor capillaries in general have wide interendothelial junctions, a large number of fenestrae and transendothelial channels formed by vesicles, and discontinuous or absent basement mem-

brane (15). Thus, tumor vessels will display increased permeability for large-molecular-mass substances compared with that in normal vessels (16). Moreover, the interstitial space of tumors is generally much larger than that of normal tissues (17).

In this methodologic study, we therefore present a more comprehensive approach to the analysis of dynamic CT scans, which makes it possible to estimate regional blood flow, capillary permeability, and relative compartmental volumes. This is achieved by detecting and analyzing not only the initial phase of the contrast enhancement but also its further evolution over a period of some minutes.

MATERIALS AND METHODS

CT System and Noise Characteristics

Imaging was performed on a clinical CT scanner (Somatom Plus 4; Siemens Medical Systems, Erlangen, Germany). CT scanning parameters were 0.5-second acquisition time, 120-kV tube voltage, 50-mA tube current, 8-mm-thick sections, no gantry tilt, and a standard adult body kernel (AB50). To evaluate pixel noise and interscan variability for these acquisition parameters, a series of 40 CT scans was acquired with a repetition time of 10 seconds from the same section of a water-filled Lucite cylinder ($\phi = 20.0$ cm). For each reconstructed image, the mean value and the SD (pixel noise) of the CT attenuation values were determined within a circular 50-mm-diameter region of interest. Moreover, the SD of the mean values over all frames was calculated (interscan variability).

Patients and Scanning Procedure

Six male patients (mean age, 49.7 years \pm 9.7 [SD]) with squamous cell carcinoma of the oro- and/or hypopharyngeal region underwent imaging before combined radiation and chemotherapy. Tumor stage was T4 N2b ($n = 2$), T4 N2c ($n = 2$), and T4 N3 ($n = 2$). The widest diameter of the tumors was between 3 and 8 cm. Written informed consent was obtained from all patients after the nature of the procedure had been fully explained to them. Institutional review board approval has been obtained for our entire study on accelerated hyperfractionated radiation and chemotherapy for patients with advanced cancer of the oro- or hypopharyngeal region, to include treatment and various invasive and noninvasive diagnostic procedures.

After acquisition of three nonenhanced images, 50 mL of a nonionic iodinated con-

trast medium (iopromide, Ultravist 300; Schering, Berlin, Germany) was administered within 30 seconds via an indwelling forearm canula by using a computer-aided, volumetric pump system (CAI; Doltron, Uster, Switzerland). Starting with the contrast material infusion, sequential CT scans were obtained from the same section with the previously mentioned parameters with a repetition time of 5 seconds for a total of 90 seconds (18 scans) and a repetition time of 15 seconds up to a total scanning time of 6 minutes (18 additional scans). The effective dose per scan was 0.005 mSv (18), resulting in a total effective dose of less than 0.2 mSv per examination.

Image Postprocessing and Data Analysis

Image postprocessing was performed off-line on a personal computer with a Pentium 200 processor under the operating system (Windows-NT, version 4.0; Microsoft, Redmond, Wash) by using IDL (Interactive Data Language, version 3.6; Research Systems, Boulder, Co). For quantitative analysis of the dynamic CT images, regions of interest were defined over the tumor, the carotid artery, and the neck muscles (semispinal muscle of head, splenius muscle of head, or splenius muscle of neck). In general, advanced squamous cell carcinomas of the neck are not well defined at CT; the necrotic and viable parts of the tumors often infiltrate the surrounding muscles and can be hard to distinguish from normal tissue. We, therefore, analyzed only parts of the tumor where the available dynamic and the consecutively measured staging CT scans showed no suggestion of non-tumor or necrotic tissue. The muscle region of interest was chosen as large as possible.

The CT attenuation, H_T , (in Hounsfield units) of soft-tissue regions was estimated by computing the mean of all pixel values in each region of interest. This approach, however, has been proved to be inadequate for the evaluation of the CT attenuation of blood, H_B , from the carotid arteries. Owing to the small size of these vessels, even small patient movements during the measurement period can result in a displacement of the arteries relative to the region of interest. To take this problem into account, we calculated the 90th percentile, instead of the mean, of all pixel values in the region of interest to estimate the actual CT attenuation, H_B , in the arteries. This allowed the definition of larger regions of interest, which reduced the probability that the region of interest did not completely coincide with the vessel due to patient movements.

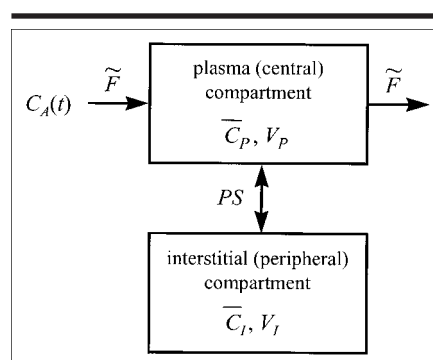


Figure 1. Open two-compartment model to describe the transport of a contrast medium through the capillaries and its bidirectional diffusion between plasma (mean concentration, \bar{C}_p ; volume, V_p) and interstitial space (mean concentration, \bar{C}_i ; volume, V_i). $C_A(t)$ is the concentration in a tissue-feeding artery, \bar{F} the apparent capillary plasma flow, and PS the permeability-surface area product.

From the CT attenuation values, the mean concentrations of the extracellular contrast agent in the tissue \bar{C}_T and in arterial blood plasma \bar{C}_A (the arterial input function) were calculated from

$$\bar{C}_T = k \cdot (H_T - H_T^{\text{pre}}) \text{ and}$$

$$\bar{C}_A = \frac{k}{1 - h_{mv}} \cdot (H_B - H_B^{\text{pre}}) \quad (1)$$

where H_T^{pre} and H_B^{pre} are the precontrast values in tissue and blood, respectively, $h_{MV} \approx 0.45$ is the hematocrit in major vessels, and k is a calibration factor. To improve the signal-to-noise ratio of the curves, they were filtered outside the peak region employing a median filter with a width of three data points.

The pharmacokinetic model employed for the analysis of the concentration-time courses is shown in Figure 1. A list of symbols used in this study is presented in Table 1. According to the open two-compartment model, the transport of a contrast medium through the plasma compartment (with mean contrast agent concentration \bar{C}_p and volume V_p) and its diffusion into the interstitial space (with mean concentration \bar{C}_i and volume V_i) can be described with the following pair of mass balance equations:

$$V_p \frac{d\bar{C}_p(t)}{dt} = \bar{F}(C_A - \bar{C}_p) - PS(\bar{C}_p - \bar{C}_i) \quad (2)$$

and

$$V_i \frac{d\bar{C}_i(t)}{dt} = PS(\bar{C}_p - \bar{C}_i), \quad (3)$$

TABLE 1
Symbols and Definitions

\bar{C}_A	Mean concentration of contrast in arterial blood plasma (grams per milliliter)
\bar{C}_i	Mean concentration of contrast in the interstitial compartment (grams per milliliter)
\bar{C}_T	Mean concentration of contrast in tissue (grams per milliliter)
\bar{C}_p	Mean concentration of contrast in the (tissue) plasma compartment (grams per milliliter)
F	Plasma flow (milliliters per minute)
\bar{F}	Apparent plasma flow (milliliters per minute)
f_i	Relative volume fraction of the interstitial compartment
f_p	Relative volume fraction of the (tissue) plasma compartment
H_B	CT attenuation of blood (Hounsfield units)
H_T	CT attenuation of tissue (Hounsfield units)
h_{mv}	Hematocrit in major vessels
h_{sv}	Hematocrit in small vessels
m	Tissue mass (grams)
PS	Permeability-surface area product (milliliters per minute)
rBF	Regional blood flow (milliliters per minute per 100 g)
rBV	Regional blood volume (milliliters per 100 g)
ρ	Tissue density (grams per cubic centimeter)
V_i	Volume of the interstitial compartment (milliliters)
V_p	Volume of the (tissue) plasma compartment (milliliters)
V_T	Tissue volume (milliliters)

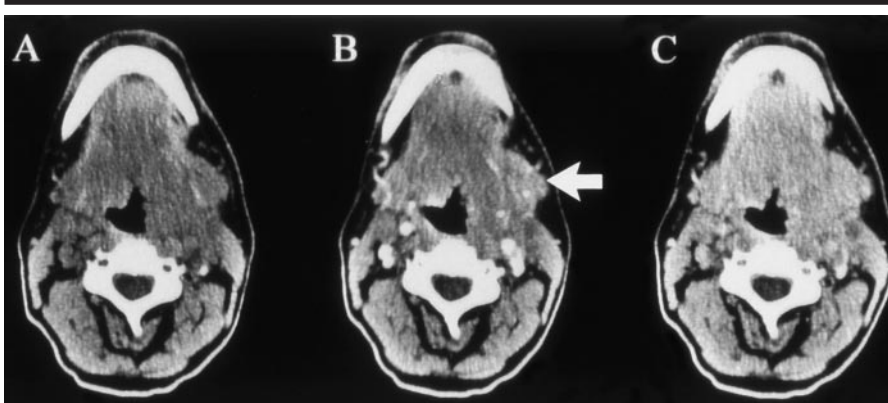


Figure 2. Patient 1. Three of 39 rapid transverse CT images from a dynamic CT data set obtained in a 40-year-old man with a squamous cell carcinoma (T4 N2c). The images were acquired with the same window scaling A, before; B, 30 seconds after; and C, 150 seconds after the onset of a 30-second-long, constant-rate administration of contrast agent. They demonstrate an advanced tumor (arrow in B) on the left, which asymmetrically compresses the hypopharyngeal region. The concentration-time courses determined from the carotid artery and from the tumor are shown in Figure 4a and 4b, respectively.

where $C_A(t)$ is the concentration of the contrast agent in an artery, \bar{F} the apparent capillary plasma flow, and PS the permeability-surface area product. A more rigorous derivation of this model, which takes spatial variations of the contrast agent concentration along the capillaries into account, is given in the Appendix. It reveals that the apparent plasma flow $\bar{F} = F/r$ ($0 \leq r \leq 1$) is always higher than the true plasma flow F . The total tissue concentration \bar{C}_T , which is related to the measurable increase in the CT attenuation according to Equation (1), is given with

$$\bar{C}_T(t) = f_p \bar{C}_p(t) + f_i \bar{C}_i(t), \quad (4)$$

where $f_p = V_p/V_T$ and $f_i = V_i/V_T$ are the relative fractions of the plasma and the interstitial distribution space within the examined tissue volume V_T , respectively.

Pharmacokinetic data analysis was performed with an extended least-squares modeling program package (MKMODEL, version 5.0; Biosoft, Cambridge, England) by means of the model described with Equations (2)–(4). The algorithm employed for the numeric integration of the two coupled differential equations is based on the Kutta-Merson method (19,20), whereby step size selection and local error control are provided automatically. With this approach, an estimate for the

following set of independent tissue parameters was obtained from the concentration-time courses $\bar{C}_T(t)$ and $\bar{C}_A(t)$: \bar{F}/V_p , PS/V_p , f_p and f_i . The fifth model parameter is given with $PS/V_i = PS/V_p \cdot f_p/f_i$. The errors in the final fit parameters were computed by means of the covariance matrix.

To be comparable with data presented by other groups, the regional blood volume per unit tissue mass, rBV (in milliliters per 100 g), and the apparent regional blood flow per unit tissue mass, rBF (in milliliters per minute per 100 g), were computed according to

$$\text{rBV} = \frac{V_p}{(1 - h_{sv}) \cdot m} = \frac{f_p}{(1 - h_{sv}) \cdot \rho} \quad (5)$$

and

$$\text{rBF} = \frac{\bar{F}}{(1 - h_{sv}) \cdot m} = \text{rBV} \cdot \frac{\bar{F}}{V_p}, \quad (6)$$

where $h_{sv} \approx 0.25$ (21) is the hematocrit in small vessels and $m = \rho \cdot V_T$ is the mass of the soft tissue with mass density $\rho = 1.04 \text{ g/cm}^3$ in the examined tissue volume V_T .

RESULTS

The evaluation of the low-dose CT images acquired from the phantom yielded a pixel noise of $\pm 14 \text{ HU}$. Thus, (soft-tissue) regions of interest should comprise at least 800 pixels to reduce the SEM of the CT attenuation below $\pm 0.5 \text{ HU}$. The variation in the mean attenuation values over all scans was $\pm 0.3 \text{ HU}$. In muscle tissue, on the other hand, we estimated values of ± 15 and $\pm 1.7 \text{ HU}$ for both parameters, respectively. The increased interscan variability in the neck muscles is mainly caused by swallowing.

As a representative sample of a patient study, Figure 2 shows three of 39 rapid transverse CT images of a dynamic CT data set acquired in a patient with a hypopharyngeal carcinoma.

Contrast enhancement determined in muscle tissue from the low-dose CT scans was less than 14 HU and, thus, the concentration-time courses could not be analyzed on an individual basis with the proposed pharmacokinetic model due to the high interscan variability. To overcome this limitation, the individual concentration-time courses determined for muscle and blood were averaged over all patients. The resultant curves are shown in Figure 3. The blood curve (Fig 3a) demonstrated a nearly linear increase during the constant-rate, contrast agent administration over 30 seconds, followed by a biexponential decrease immediately

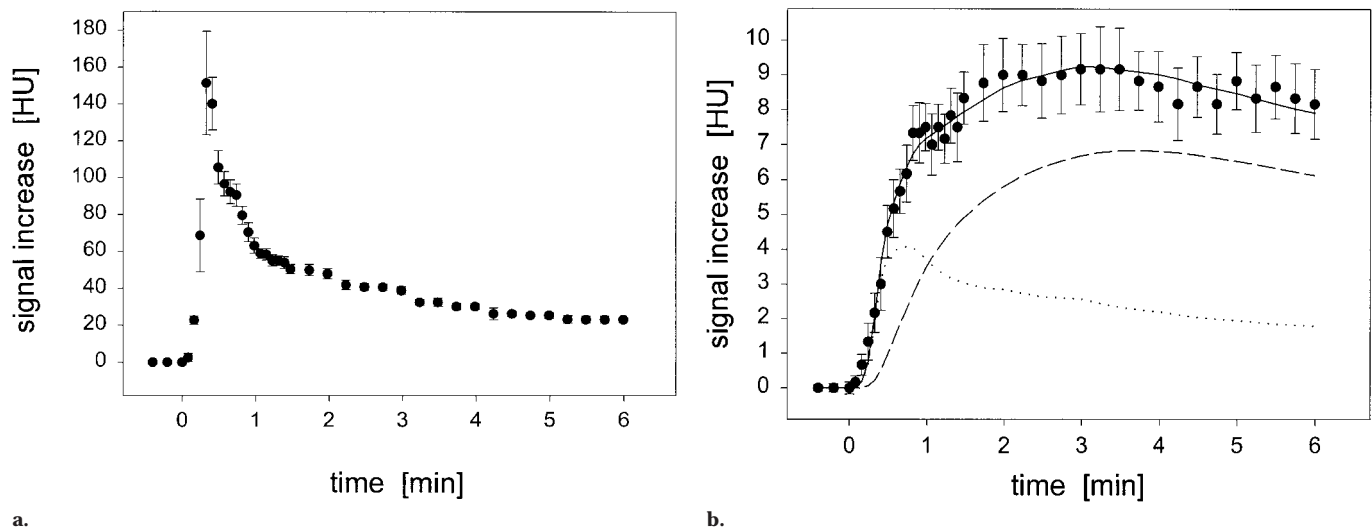


Figure 3. Concentration-time courses determined (a) from the carotid artery and (b) from neck muscle tissue. Both curves were averaged over six patients. ● indicates mean value, and the error bars indicate the SEM of the individual concentration values. The curves in b show the result of the nonlinear regression analysis (solid line, total tissue concentration \bar{C}_T ; dotted line, intravascular contribution $f_p \cdot \bar{C}_p$; broken line, interstitial contribution $f_i \cdot \bar{C}_i$). The estimated model parameters are given in Results.

after its end. The concentration-time profile measured in muscle tissue (Fig 3b), on the other hand, revealed a more complex pattern: After a fast initial increase during the period of contrast agent administration, the increase became smaller and the tissue concentration reached a maximum at about 3 minutes after contrast agent infusion. As demonstrated in Figure 3b, this behavior can be described by separating the bulk tissue concentration into its plasma and interstitial component. The non-linear regression analysis yielded the following tissue parameters: $f_p = 0.04 \text{ mL/mL} \pm 0.01$, $f_i = 0.12 \text{ mL/mL} \pm 0.01$, $\bar{F}/V_p = 2.5 \text{ mL/mL/min} \pm 0.9$, and $PS/V_p = 1.6 \text{ mL/mL/min} \pm 0.6$. The corresponding muscle regional blood flow and regional blood volume values are given in Table 2 together with values determined by other groups with different techniques.

The increase in CT attenuation observed in the six neck tumors after iopromide administration was markedly higher than that found in muscle tissue and, thus, the tumor curves could be analyzed individually by using the corresponding individual arterial input function. Two typical cases are presented in Figure 4, revealing that the tumor curves can adequately be described with the proposed model. The model parameters determined for all tumors are summarized in Table 3 together with the corresponding mean values and SDs.

DISCUSSION

The pharmacokinetic model employed in the present study takes into consider-

TABLE 2
Comparison of Muscle Blood Flow and Volume Estimated in Different Studies with Different Measurement Techniques

Reference	Technique	Subjects	Muscle Region	Status	rBF (mL/min/100 g)	rBV (mL/100 g)
Present study	Dynamic CT	Human	Neck	Undefined	12.0 ± 5.4	4.9 ± 1.3
22	Plethysmography	Human	Forearm	Rest	3.7 ± 1.6	NM
23	Plethysmography	Human	Forearm	Rest	4.1 ± 2.1	NM
24	PET	Human	Calf	Rest	2.1 ± 1.1	NM
				Exercise	13.5 ± 3.3	NM
25	PET	Human	Femoral	Rest	3.1 ± 1.6	3.3 ± 0.7
			Posterior	Rest	5.8 ± 1.0	4.7 ± 0.6
			Anterolateral	Rest	4.1 ± 1.3	3.1 ± 0.3
26	PET	Rabbit	Leg	Rest	7.0 ± 1.0	1.8 ± 0.1
27	PET	Rabbit	Thigh	Rest		

Note.—NM = not measured, PET = positron emission tomography.

ation both capillary blood supply ($\bar{F}/V_p = \text{rBF/rBV}$) (Eq [6]) and exchange of contrast medium between the plasma and the interstitial tissue compartment (PS/V_p). Thus, it combines aspects of the perfusion model of Miles and of the permeability models formulated by Tofts et al (29,30) and by our group (31,32).

The kinetics of contrast enhancement observed in this study with sequential CT scanning in muscle (Fig 3) and tumor tissue (Fig 4) can be described adequately with the proposed compartmental model. The decomposition of the bulk tissue curves into their plasma and interstitial components demonstrates that the initial (perfusion) phase is dominated by the contrast agent in the intravascular compartment (permeability-limited transport, $PS/F < 1$) and, thus, can be used to

estimate tissue perfusion in a reasonably good approximation as, for example, using the steepest-gradient technique. However, if the contrast enhancement is not permeability limited, the steepest-gradient technique may result in a marked overestimation of blood flow. Moreover, the decomposition of the contrast-enhancement curves reveals that the intravascular component cannot be neglected, as is the case in the previously mentioned simple permeability models. The differences in the tumor enhancement profiles shown in Figure 4b and 4d, for example, are mainly due to differences in the intravascular component, whereas the interstitial contribution is nearly identical.

To roughly examine the validity of our approach, attenuation-time courses were measured in normal neck muscles of six

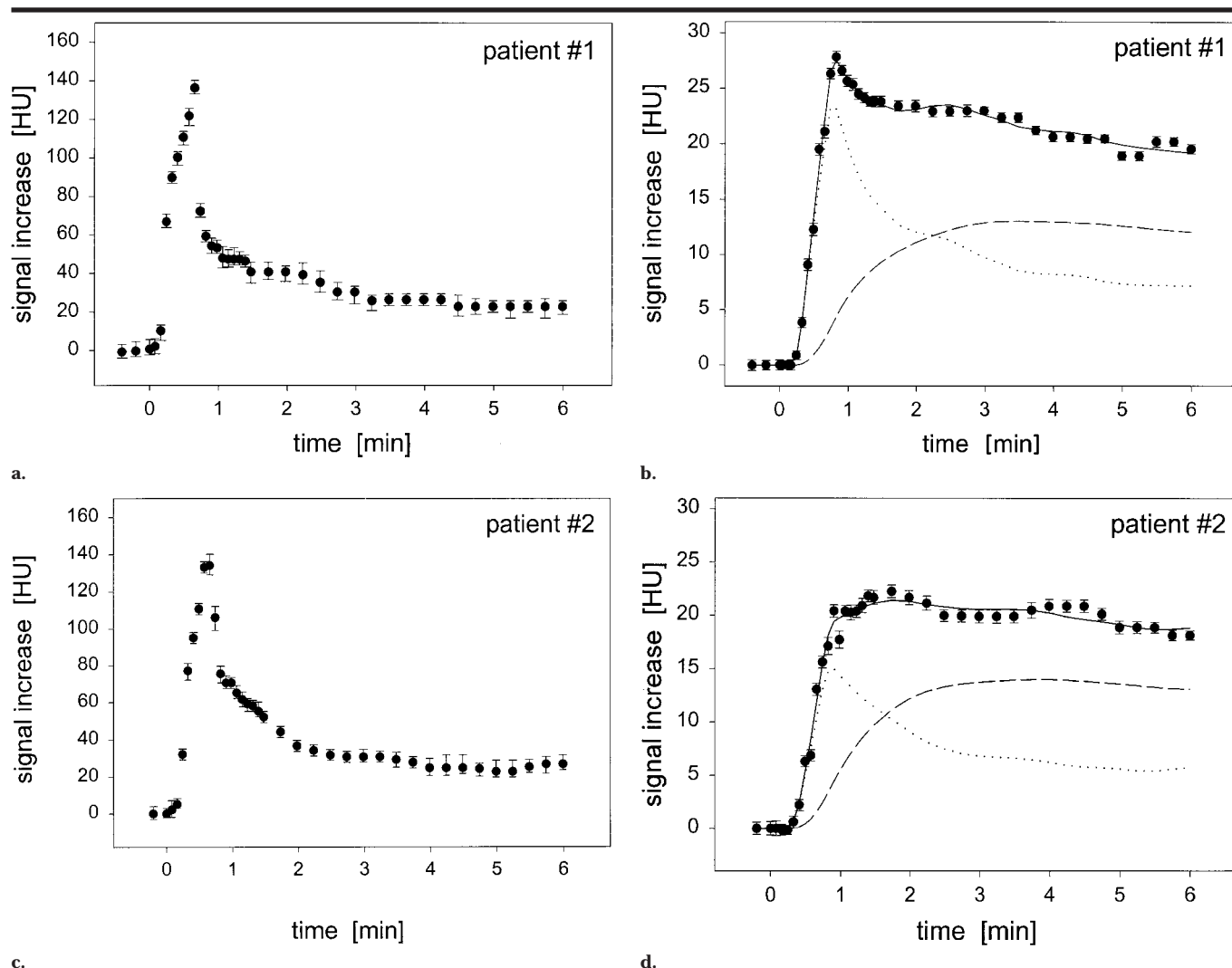


Figure 4. Patients 1, 2. (a–d) Concentration-time courses determined in two patients from a region of interest over (a, c) the carotid artery (● indicates the 90th percentile, and the error bars indicate the 95% CIs [28]) and (b, d) the neck tumor (● indicates the mean value, and the error bars indicate the SEM). The curves show the results of the nonlinear regression analysis (solid line, total tissue concentration \bar{C}_T ; dotted line, intravascular contribution $f_p \cdot \bar{C}_p$; broken line, interstitial contribution $f_i \cdot \bar{C}_i$). The estimated model parameters are given in Table 3.

TABLE 3
Pharmacokinetic Parameters Determined in Neck Tumors

Patient No.	f_p	f_i	\bar{F}/V_p (mL/mL/min)	PS/V_p (mL/mL/min)	rBF (mL/100 g)	rBF (mL/min/ 100 g)
1	0.17 ± 0.01	0.25 ± 0.01	2.9 ± 0.3	0.59 ± 0.08	22 ± 1	63 ± 7
2	0.12 ± 0.02	0.27 ± 0.02	2.5 ± 0.7	0.95 ± 0.25	16 ± 2	38 ± 12
3	0.12 ± 0.01	0.30 ± 0.06	3.8 ± 0.5	0.37 ± 0.06	15 ± 1	59 ± 8
4	0.10 ± 0.01	0.29 ± 0.07	2.9 ± 0.7	0.55 ± 0.19	13 ± 2	37 ± 11
5	0.15 ± 0.02	0.29 ± 0.02	2.8 ± 0.5	0.77 ± 0.20	19 ± 2	53 ± 11
6	0.12 ± 0.04	0.24 ± 0.03	1.4 ± 0.6	1.09 ± 0.69	16 ± 5	22 ± 12
Mean \pm SD	0.13 ± 0.02	0.27 ± 0.02	2.7 ± 0.8	0.72 ± 0.27	17 ± 3	45 ± 16

patients and the regional blood volume and regional blood flow values derived were compared with results obtained by other groups with various measurement techniques (Table 2). The regional blood

volume value of $4.9 \text{ mL}/100 \text{ g} \pm 1.3$ determined with our CT technique is slightly higher than the literature values, which are in the range between $1.8 \text{ mL}/100 \text{ g} \pm 0.1$ and $4.7 \text{ mL}/100 \text{ g} \pm 0.6$. This

may be explained (a) by the fact that the neck muscles—in contrast to the muscles of the leg or forearm—were not at rest since the patients were instructed not to move their heads during the examination period and (b) by a small vasodilatory effect of the employed nonionic contrast medium (33,34). The relative fractions of the plasma ($f_p = 0.04 \text{ mL/mL} \pm 0.01$) and interstitial tissue compartment ($f_i = 0.12 \text{ mL/mL} \pm 0.01$) also coincide well with scarce literature data available for muscle tissue. For skeletal muscle of the rat, O'Connor and Bale (35) reported a relative fraction of the interstitial volume of $0.14 \text{ mL/mL} \pm 0.02$ and Gullino et al (36) a relative volume of the extracellular space ($\cong f_p + f_i$) of $0.16 \text{ mL/mL} \pm 0.01$.

The muscle blood flow of $12.0 \text{ mL/min}/100 \text{ g} \pm 5.4$ estimated in our study, on the

other hand, is considerably higher than the data obtained by other groups, varying between 3.1 and 7.0 mL/min/100 g, but is still smaller than the blood flow value of 13.5 mL/min/100 g \pm 3.3 determined with positron emission tomography (PET) during ergometric exercise of the calf muscle (Table 3). This discrepancy is mainly due to the fact that the apparent plasma flow $\tilde{F} = F/r$ ($0 \leq r \leq 1$), which can be estimated from the measured CT enhancement profiles according to our model, is considerably higher than the true plasma flow F . With the assumption, for example, that the concentration of the contrast medium in the capillaries decreases linearly between the inlet and the outlet of a capillary, it follows that $r = 1/2$ (Appendix), which means that the apparent flow \tilde{F} is twice as high as the true flow F . However, it should be recognized that the other three model parameters (f_p , f_i , and PS/V_p) are not affected by this systematic overestimation.

The surface area of the capillaries per unit volume of skeletal muscle tissue, S/V_T , is known to be approximately 130 cm²/cm³ \pm 25 (mean \pm SEM calculated from the results of different studies summarized in a review by Jain et al [16]). From this, the mean permeability of muscle capillaries for the contrast agent iopromide (molecular mass, $A = 791$ d) can be estimated to be $P = f_p \cdot (PS/V_p)/(S/V_T) = (0.8 \pm 0.4) \cdot 10^{-5}$ cm/sec. This value fits well to permeability coefficients found in muscle tissue for Na⁺ ($P = 5.1 \times 10^{-5}$ cm/sec, $A = 11$ d), sucrose ($P = 1.4 \times 10^{-5}$ cm/sec, $A = 342$ d), and inulin ($P = 0.2 \times 10^{-5}$ cm/sec, $A = 5,000$ d) [16].

The pharmacokinetic parameters summarized in Table 3 demonstrate that both the plasma and the interstitial spaces in the examined neck tumors are much larger than those in muscle tissue ($f_p = 0.13$ mL/mL \pm 0.02 vs 0.04 mL/mL \pm 0.01, $f_i = 0.27$ mL/mL \pm 0.02 vs 0.12 mL/mL \pm 0.01). The estimated tumor volumes fit well into the range of data summarized in a comprehensive review article by Jain (17) for a variety of experimental sarcomas and carcinomas in the rat ($f_i = 0.33$ – 0.60 mL/mL), as well as for different human brain tumors ($f_p + f_i \approx 0.13$ – 0.40 mL/mL).

Results of a few studies of blood flow through squamous cell carcinoma of the head and neck region in humans have been reported. Data published until 1992 are summarized in a review article by Vaupel and co-workers (37). Despite similar histologic classification and primary site, the measured blood flow values vary considerably between 6 and 25 mL/min/

100 g. Compared with these data, the mean apparent blood flow determined in the present study of 45 mL/min/100 g \pm 16 (range, 22–63 mL/min/100 g) is considerably higher due to the reasons discussed previously. It is interesting to note, however, that the tumor-to-muscle blood flow ratio of 3.8 ± 2.2 obtained in our study is very close to the tumor-to-normal tissue ratio of 3.9 ± 2.7 determined by Wheeler and co-workers from washout curves of intraarterially injected xenon-133 (38). Relatively high blood flow values in squamous cell carcinoma of the head and neck were also reported by Hermans et al in 1997 (39). They estimated tissue perfusion from dynamic CT scans by means of the steepest-gradient technique in 18 patients and found a mean blood flow of 75 mL/min/100 g, varying between 28 and 132 mL/min/100 g.

As an interesting result, the higher regional blood flow observed in our study in the neck tumors (45 mL/min/100 g \pm 16) in comparison with that in muscle tissue (12 mL/min/100 g \pm 5) is mainly due to the higher regional blood volume and not to a higher flow per unit plasma volume \tilde{F}/V_p (Eq [6]), which is nearly identical for tumor (2.7 mL/mL/min \pm 0.8) and muscle tissue (2.5 mL/mL/min \pm 0.9). The surface-area product per unit plasma volume (PS/V_p) was also found not to be higher in the neck tumors than in muscle tissue. This is consistent with the findings of Jain (40) and Gerlowski and Jain (41) that the permeability of compounds with a molecular mass of less than 2,000 d is almost identical in normal and neoplastic tissues. As pointed out by different investigators, this makes a strong argument for the use of contrast media with large molecular mass for the assessment of abnormal capillary permeability and thus for improved tumor detection. The pharmacokinetic properties of conventional contrast agents, on the other hand, make them an ideal probe for studying the chances of circulating low-molecular-mass compounds (eg, anticancer drugs) to distribute into the interstitial space of defined tissues. This is particularly interesting for solid malignant tumors as, in this case, the delivery of systemically administered drugs to the target site is one of the major problems of drug therapy.

The tumor parameters summarized in Table 3 indicate that the relative compartmental volumes f_p and f_i can be determined with a greater accuracy and, moreover, show a smaller interindividual variation than the functional parameters characterizing the transport and extrava-

sation of the applied contrast medium (\tilde{F}/V_p and PS/V_p). Whereas the first observation mainly reflects the numeric robustness of the nonlinear parameter estimation against measurement errors, the second observation reveals that functional variability between tumors is larger than are structural or histologic variability. This is in accordance with all available information on parameters characterizing microcirculation in human cancer. According to these data, marked variations in physiologic properties are likely to occur between tumors with the same grade and clinical stage and, moreover, between different locations within a tumor (42). Owing to this reason, care must be exercised when comparing parameters obtained for tumors in different individuals (16). Despite the fact that the physiologic tissue parameters estimated in the present study agree well with published data, it will thus be necessary in future studies to experimentally validate our perfusion-permeability model in more detail on an individual basis. In an animal study, for example, CT measurements of blood flow in normal tissues and in transplanted tumor models can be correlated with flow values determined by means of simultaneously injected radiolabeled microspheres. Moreover, the relative volume of the intravascular and the extracellular space can be estimated by means of gamma counting of tissue samples after in vivo administration of a radiotracer confined to blood vessels and of another one excluded by cells.

Independent of whether our model can be validated with such experiments in all details, it offers promising prospects for the clinical radiologist to quantitatively characterize tissue microcirculation. It is, for example, a fundamental concept in oncology that tumor growth and metastatic potential depend on the ability of a tumor to induce formation of new microvessels (43–45), often with severe structural abnormalities (15,16,46). It is therefore speculated that monitoring of tumor neovascularization might make it possible to predict tumor aggressiveness (eg, risk of lymphatic involvement and disease-free survival after therapy) and to design an individually tailored therapeutic approach (45,47–51). As a result of a compromised and heterogeneous microcirculation, many human malignancies comprise hypoxic tissue areas that may lead to a failure of conventional radiation therapy (46,52). Such hypoxic tumors need to be identified and selected for special procedures that exist for dealing with hypoxic cells but cannot be em-

ployed in all patients (39). Since tissue perfusion is correlated with tissue oxygenation, individual radiation therapy planning might be possible in the future on the basis of physiologic parameters determined with noninvasive sequential CT.

The pharmacokinetic model derived in this study can also be employed to analyze dynamic MR measurements for administration of a diffusible paramagnetic MR contrast agent (53). Findings in first applications in dynamic MR mammography showed that the large variety of enhancement patterns observed in different breast tissues (eg, glandular tissue, mastopathic nodules, fibroadenomas, carcinomas) can adequately be parameterized with our perfusion-permeability model. Up to now, however, it is an open question as to what extent the diffusive behavior of water protons or the variation of proton relaxivities in different tissue compartments affect the reliability of functional tissue parameters determined from dynamic MR images (54). Since there are MR and CT contrast media with similar physicochemical properties, it may be possible to answer these questions with a comparative analysis of dynamic CT and MR data sets acquired in the same patients.

One limitation of the dynamic CT technique is undoubtedly its radiation exposure for the patient. Despite the fact that the dose per scan was reduced as far as possible in our study (25 mAs) the total effective dose may still be too high for a diagnostic procedure under certain circumstances. It should be recognized, however, that a comparable extensive quantitative characterization of tissue microcirculation can otherwise be obtained only with multitracer PET studies, which lead to a markedly higher radiation exposure and, moreover, in general make it necessary to take arterial blood samples in short time intervals to determine the arterial input function of the applied tracers.

In clinical practice, one may also be faced with the problem that dynamic CT scans can be acquired with a sufficiently high temporal resolution from only one section. It may thus be difficult in certain cases to determine the arterial input function, since a large vessel is not in the field of view. With the advent of a new generation of CT scanners with multirow detectors, however, it will be possible in the near future to determine blood and tissue curves from different sections.

In conclusion, the proposed pharmacokinetic analysis of dynamic CT data offers promising prospects to quantitatively assess tissue microcirculation with physiologic parameters, concretely with the re-

gional blood flow, the capillary permeability, and relative compartmental volumes. Although our approach is not yet validated in all details, the agreement of our results with published data indicates that it may be employed in patient studies to improve our understanding of tissue pathophysiology and of the action and optimization of therapeutic interventions.

■ APPENDIX

The following analysis is based on a single-capillary model, which assumes identical capillaries in the examined tissue. Furthermore, we assume that the solubility of the employed extracellular contrast medium in the interstitial fluid is the same as that in plasma and that the permeability is the same in both directions across the capillary wall (passive transport). With these assumptions, the transport of a contrast medium through the capillaries and its diffusion into the interstitial space can be described with the following pair of mass balance equations derived from the Fick first law (55):

$$V_p \frac{\partial C_p(t, x)}{\partial t} = -F \cdot L \frac{\partial C_p(t, x)}{\partial x} - PS[C_p(t, x) - C_1(t, x)] \quad (A1)$$

and

$$V_1 \frac{\partial C_1(t, x)}{\partial t} = PS[C_p(t, x) - C_1(t, x)], \quad (A2)$$

where $C_p(t, x)$ is the contrast agent concentration in plasma at time t and at point x along a capillary (of length L and volume V_p), and $C_1(t, x)$ is the concentration of the contrast agent in the interstitial compartment (volume V_1). F is the plasma flow through the capillary, and PS is the permeability-surface area product. To arrive at a compartmental model, spatial variations are suppressed by integrating Equations (A1) and (A2) from inlet ($x = 0$) to outlet ($x = L$), so that

$$\int_0^L C_p(t, x) dx = L \cdot \bar{C}_p(t),$$

$$\int_0^L C_1(t, x) dx = L \cdot \bar{C}_1(t), \text{ and}$$

$$\int_0^L (\partial C_p / \partial x) dx = C_p(L) - C_p(0) \quad (48).$$

Thus,

$$V_p \frac{d\bar{C}_p(t)}{dt} = F(C_A - C_V) - PS(\bar{C}_p - \bar{C}_1) \quad (A3)$$

and

$$V_1 \frac{d\bar{C}_1(t)}{dt} = PS(\bar{C}_p - \bar{C}_1) \quad (A4)$$

with the arterial and venous contrast agent concentrations $C_A(t) = C_p(t, x = 0)$ and $C_V(t) = C_p(t, x = L)$, respectively. Equations (A3) and (A4), however, cannot be solved directly since the venous concentration $C_V(t)$ is difficult to measure. Therefore, additional assumptions must be made to simplify the problem.

One approach was presented by Kety (56) for inert gases that are rapidly distributed in the interstitial and intracellular spaces. Since the capillary volume represents less than 5% of the volume in most tissues, it is reasonable to assume that changes in the mean tissue concentration of the tracer during the time of passage of an element of blood through the tissue is negligible in comparison with the concentration change occurring in the blood itself. By using this postulate, Kety derived an analytic solution for the total amount of tracer in a tissue region from which the transfer coefficient $K = F \cdot E / V_e$ can be determined with V_e the partition volume of exchangeable tracer and $E = 1 - e^{-PS/F}$ the extraction fraction. Whereas the Kety model can also be applied to activity-time courses measured with PET after the administration of oxygen-15-labeled water, it is *not* applicable to extracellular contrast media usually employed in CT and MR imaging studies. In contrast to inert gases or O-15-labeled water, these contrast media are distributed within only the interstitial volume, which represents less than about 20% of the total volume in tissues. Thus, changes in the mean tissue concentration of the tracer during the passage of an element of blood cannot be ignored.

An alternative approach was presented by Morales and Smith (57). These authors assumed only that the difference $C_A - \bar{C}_p$ between the arterial and the mean capillary contrast agent concentration is some constant fraction $0 \leq r \leq 1$ of the difference $C_A - C_V$ between the arterial and venous concentrations, that is,

$$C_A - C_V = \frac{1}{r} (C_A - \bar{C}_p). \quad (A5)$$

Substitution into Equation (A3) yields

$$V_p \frac{d\bar{C}_p(t)}{dt} = \tilde{F}(C_A - \bar{C}_p) - PS(\bar{C}_p - \bar{C}_1), \quad (A6)$$

with $\tilde{F} = F/r \geq F$ describing the *apparent* plasma flow. A graphic visualization of

the mathematic model defined with the two coupled differential Equations (A6) and (A4) for \bar{C}_p and \bar{C}_t is given in Figure 1. In contrast to the Kety model, the approach formulated by Morales and Smith makes it possible to independently characterize plasma flow *and* diffusion across capillary endothelium. The rate of these transport processes is described with the apparent plasma flow \bar{F} and the permeability-surface area product PS , respectively.

Acknowledgment: We thank Robert Lucht, PhD, and Joachim Zaers, MS, for their helpful contributions and the support they have given to this study.

References

1. Axel L. Cerebral blood flow determination by rapid-sequence computed tomography. *Radiology* 1980; 137:679-686.
2. Berninger WH, Axel L, Norman D, Napel S, Redington RW. Functional imaging of the brain using computed tomography. *Radiology* 1981; 138:711-716.
3. Norman D, Axel L, Berninger WJ, et al. Dynamic computed tomography of the brain: techniques, data analysis and applications. *AJR* 1981; 136:759-770.
4. Hopper JL, Davis SD, Tress BM, Kaye AH, Rossiter SC, Derrick PL. Analysis of dynamic computed tomography scan brain images. *Invest Radiol* 1987; 22:651-657.
5. Nambu K, Takehara R, Terada T. A method of regional cerebral blood perfusion measurement using dynamic CT with an iodinated contrast medium. *Acta Neurol Scand* 1996; 166(suppl)28-31.
6. Rosen BR, Belliveau JW, Chien D. Perfusion imaging by nuclear magnetic resonance. *Magn Reson Q* 1989; 5:263-281.
7. Rempp K, Brix G, Wenz F, Becker C, Gückel F, Lorenz WJ. Quantitative assessment of cerebral blood flow and volume by dynamic susceptibility enhanced MR imaging. *Radiology* 1994; 193:637-641.
8. Ostergaard L, Weiskoff RM, Chesler DA, Gyldensted C, Rosen BR. High resolution measurements of cerebral blood flow using intravascular tracer bolus passages. I. Mathematical approach and statistical analysis. *Magn Reson Med* 1996; 36:715-725.
9. Schreiber W, Gückel F, Stritzke P, Schmiedek P, Schwarz A, Brix G. Cerebral blood flow and cerebrovascular reserve capacity: absolute quantification by dynamic magnetic resonance imaging. *J Cereb Blood Flow Metab* 1998; 18:1143-1156.
10. Miles KA. Measurement of tissue perfusion by dynamic computed tomography. *Br J Radiol* 1991; 64:409-412.
11. Peters AM, Gunasekera RD, Henderson BL, et al. Non-invasive measurements of blood flow and extraction fraction. *Nucl Med Commun* 1987; 8:823-837.
12. Blomley MJ, Coulson R, Bufkin C, Lipton MJ, Dawson P. Contrast bolus dynamic computed tomography for the measurement of solid organ perfusion. *Invest Radiol* 1993; 28(suppl):S72-S77.
13. Miles KA, Hayball MP, Dixon AK. Functional images of hepatic perfusion obtained with dynamic CT. *Radiology* 1993; 188:405-411.
14. Miles KA, Hayball MP, Dixon AK. Measurement of human pancreatic perfusion using dynamic computed tomography with perfusion imaging. *Br J Radiol* 1995; 68:471-475.
15. Jain RK. Determinants of tumor blood flow: a review. *Cancer Res* 1988; 48:2641-2658.
16. Jain RK. Transport of molecules across tumor vasculature. *Cancer Metastasis Rev* 1987; 6:559-593.
17. Jain RK. Transport of molecules in the tumor interstitium: a review. *Cancer Res* 1987; 47:3039-3051.
18. Kalender W, Schmidt B, Zanki M, Schmidt M. A PC program for estimating dose and effective dose values in computed tomography. *Eur Radiol* (in press).
19. Crosbie RE, Hayes W. Variable-step integration methods for simulation applications. *Appl Math Modeling* 1976; 1:137-140.
20. Sparks LE. Variable step size Runge-Kutta technique for solving initial value problems. *Access* 1983; Jan/Feb:30-34.
21. Gaetgens P. Physiologie des lutes. In: Deetjem P, Speckmann EJ, eds. *Physiologie*. Munich, Germany: Urban & Schwarzenberg, 1992; 261-290.
22. Cooper KE, Edholm OG, Mottram RF. The blood flow in skin and muscle of the human forearm. *J Physiol* 1955; 128:258-268.
23. Weber F, Anlauf M, Serebrenic M. Noninvasive, quantitative determination of muscle blood flow in man by a combination of venous-occlusion plethysmography and computed tomography. *Basic Res Cardiol* 1988; 83:327-341.
24. Burchert W, Schellong S, van den Hoff J, Meyer GJ, Alexander K, Hundeshagen H. Oxygen-15-water PET assessment of muscular blood flow in peripheral vascular disease. *J Nucl Med* 1996; 37:93-98.
25. Ruotsalainen U, Raitakari M, Nuutila P, et al. Quantitative blood flow measurement of skeletal muscle using oxygen-15-water and PET. *J Nucl Med* 1997; 38:314-319.
26. Kairento AL, Brownell GL, Schluederberg J, Elmaleh DR. Regional blood-flow measurements in rabbit soft-tissue tumor with positron imaging using the $C^{15}O_2$ steady-state and labeled microspheres. *J. Nucl Med* 1983; 24:1135-1142.
27. Senda M, Fischman AJ, Weise S, et al. Regional perfusion, oxygen metabolism, blood volume and immunoglobulin G accumulation at focal sites of infection in rabbits. *Eur J Nucl Med* 1992; 19:166-172.
28. Sachs L. *Angewandte statistik*. 7th ed. Berlin, Germany: Springer-Verlag, 1992; 338.
29. Tofts PA, Kermode AG. Measurement of the blood-brain barrier permeability and leakage space using dynamic MR imaging. I. Fundamental concepts. *Magn Reson Med* 1991; 17:357-367.
30. Tofts PS, Berkowitz B, Schnall MD. Quantitative analysis of dynamic Gd-DTPA enhancement in breast tumors using a permeability model. *Magn Reson Med* 1995; 33:564-568.
31. Brix G, Semmler W, Port R, Schad LR, Layer G, Lorenz WJ. Pharmacokinetic parameters in CNS Gd-DTPA enhanced MR imaging. *J Comput Assist Tomogr* 1991; 15:621-628.
32. Hoffmann U, Brix G, Knopp MV, Hess T, Lorenz WJ. Pharmacokinetic mapping of the breast: a new method for dynamic MR mammography. *Magn Reson Med* 1995; 33:506-514.
33. Pugh ND, Hutcheson IR, Edwards DH, Nossen JO, Karlsson JO, Griffith TM. Angiographic contrast media relax isolated rabbit aorta through an endothelium-independent mechanism that may not depend on the presence of the iodine atom. *Br J Radiol* 1995; 68:23-26.
34. Szolar DH, Saeed M, Flueckiger F, et al. Effects of iopromide on vasoactive peptides and allergy-mediated substances in healthy volunteers. *Invest Radiol* 1995; 30:144-149.
35. O'Connor SW, Bale WF. Accessibility of circulating immunoglobulin G to the extravascular compartments of solid rat tumors. *Cancer Res* 1984; 44:3719-3723.
36. Gullino PM, Grantham FH, Smith SH. The interstitial water space of tumors. *Cancer Res* 1965; 25:727-731.
37. Vaupel P, Schlenger K, Hoekel M. Blood flow and tissue oxygenation of human tumors: an update. *Adv Exp Med Biol* 1992; 317:139-151.
38. Wheeler RH, Ziessman HA, Medvec BR, et al. Tumor blood flow and systemic shunting in patients receiving intraarterial chemotherapy for head and neck cancer. *Cancer Res* 1986; 46:4200-4204.
39. Hermans R, Lambin P, van den Bogaert W, Haustermans K, Van der Gooten A, Baert AL. Non-invasive tumor perfusion measurement by dynamic CT: preliminary results. *Radiother Oncol* 1997; 44:159-162.
40. Jain RK. Mass and heat transfer in tumors. *Adv Transport Proc* 1984; 3:205-339.
41. Gerlowski LE, Jain RK. Microvascular permeability of normal and neoplastic tissues. *Microvasc Res* 1986; 31:288-305.
42. Vaupel P. Physiological properties of malignant tumours. *NMR Biomedicine* 1992; 5:220-225.
43. Folkman J. Tumor angiogenesis. *Adv Cancer Res* 1985; 43:175-203.
44. Folkman J. What is the evidence that tumors are angiogenesis dependent? *J Natl Cancer Inst* 1990; 82:4-6.
45. Folkman J. Intratumoral microvessel density as a prognostic factor in cancer. *Am J Pathol* 1995; 147:9-19.
46. Vaupel P, Kallinowski F, Okunieff P. Blood flow, oxygen and nutrient supply, and metabolic microenvironment of human tumors. *Cancer Res* 1989; 49:6449-6465.
47. Weidner N, Joseph PS, William RW, Folkman J. Tumor angiogenesis and metastases: correlation in invasive breast carcinoma. *N Engl J Med* 1991; 324:1-8.
48. Toi M, Kashitani J, Tominaga T. Tumor angiogenesis is an independent prognostic indicator in primary breast cancer. *Int J Cancer* 1993; 55:371-374.
49. Hayes DE. Angiogenesis and breast cancer. *Hematol Oncol Clin North Am* 1994; 8:51-71.
50. Knopp MV, Brix G, Junkermann HJ, Sinn HP. MR mammography with pharmacokinetic mapping for monitoring of breast cancer treatment during neoadjuvant therapy. *Magn Reson Imaging Clin N Am* 1994; 2:633-658.
51. Hawighorst H, Knapstein PG, Weikel W, et al. Angiogenesis of uterine cervical carcinoma: characterization by pharmacokinetic magnetic resonance parameters and histological microvessel density with correlation to lymphatic involvement. *Cancer Res* 1997; 45:4777-4786.
52. Overgaard J. Importance of tumor hypoxia in radiotherapy: a metaanalysis of controlled clinical trials. (abstr). *Radiother Oncol* 1992; 24(suppl):S64.
53. Horvath AS, Schreiber WG, Hoffmann U, Knopp MV, Hawighorst H, Brix G. A pharmacokinetic model for quantification of the perfusion rate and capillary permeability from dynamic T1-weighted MRI (abstr). In: *Proceedings of the Sixth meeting of the International Society for Magnetic Resonance in Medicine*. Berkeley, Calif: International Society for Magnetic Resonance in Medicine, 1998; 178.
54. Roberts TPL. Physiologic measurements by contrast-enhanced MR imaging: expectations and limitations. *JMRI* 1997; 7:82-90.
55. Gjedde A. Tracer kinetics. In: Wagner H, Szabo Z, Buchanan JW, eds. *Principles of nuclear medicine*. Philadelphia, Pa: Saunders, 1995; 451-461.
56. Kety SS. The theory and applications of the exchange of inert gas at the lungs and tissues. *Pharmacol Rev* 1951; 3:1-41.
57. Morales MF, Smith RE. On the theory of blood-tissue exchange of inert gases. VI. Validity of approximate uptake expressions. *Bull Math Biophys* 1948; 10:191-200.